Research Article | Vol. 29, No. 18 / 30 Aug 2021 / Optics Express 29116
Optics EXPRESS

Generation of gradient photonic moiré lattice fields

CHUNLEI SHANG,[1,2] CHENGZHEN LU,[1,2] SIWEI TANG,[1,2] YUANMEI GAO,[1,2,3] AND ZENGRUN WEN[1,2,4]

[1] Center of Light Manipulations and Applications & Shandong Provincial Key Laboratory of Optics and Photonic Device, Shandong Normal University, Jinan, 250014, China
[2] School of Physics and Electronics, Shandong Normal University, Jinan, 250014, China
[3] gaoyuanmei@sdnu.edu.cn
[4] wenzengrun@163.com

Abstract: We designed and generated gradient photonic moiré lattice fields comprising three varying periodic moiré wavefields. Because of the common twisted angles between periodic triangular and hexagonal moiré wavefields, gradient patterns can be easily obtained through coherent superposition of hexagonal-triangular-hexagonal photonic moiré lattice fields. In addition, two specific twisted angles of $\Delta\alpha|_{C=3}$ and $\Delta\alpha|_{C=5}$ are proposed, which not only guarantee the periodicity of moiré fields but also provide an additional degree of freedom to control the structural arrangement of the gradient photonic moiré lattice fields. Further study reveals the non-diffracting character of the gradient photonic moiré lattice field generated using the holographic method. This study proposes an easy way to generate and control the structures of gradient moiré lattice fields that can be used to fabricate photonic lattices in optical storage media for light modulation.

1. Introduction

Photonic crystals with periodically modulated refractive index configurations were designed to manipulate the flow of light. Various optical phenomena have been successfully achieved using photonic crystals with varying modulation modes, including discrete diffraction, anomalous refraction, and discrete solitons, which have potential for application in optical switching and signal processing [1]. Irrespective of complex microfabrication technology, photonic lattices relying on discrete optical wavefields and photorefractive effect of storage media have been widely adopted to study optical manipulation and nonlinear optical propagations such as localization, discrete spatial solitons, and bandgap solitons [2–5]. The key to creating a photonic lattice is to design the corresponding lattice wavefield, and the multi-beam interference method has been the common mechanism for generating lattice light fields in the last two decades [6]. For two-dimensional (2D) photonic lattices, discrete diffraction-free beams have often been adopted as induced light waves. Among them, triangular, quadrangular, and hexagonal beams generated by three, four, and six plane beams located at the vertices of regular polygons, respectively, are periodic [7–9]. In addition, other quantities of plane light are superimposed to form a quasi-periodic field [10,11]. Three-dimensional (3D) induced light fields for 3D photonic lattices are easily realized by adding one on-axis plane beam on the basis of 2D nondiffracting beams [12,13].

Beyond periodic and quasi-periodic configurations, photonic crystals with gradient structures have also been studied to enhance the control of light propagation. These gradient discrete crystals have been designed for complete bandgap [14], frequency-selective tunable bending [15], and focus or self-collimate devices [16], as well as graded-index lens [17,18]. Correspondingly, researchers have focused on obtaining photonic lattice fields. M. Kumar and J. Joseph designed the intensities and phases of plane waves for hexagonal wavefields to generate gradient photonic

#434935 https://doi.org/10.1364/OE.434935
Journal © 2021 Received 22 Jun 2021; revised 13 Aug 2021; accepted 15 Aug 2021; published 25 Aug 2021

Optics EXPRESS

lattice fields with three basis structures [19]. Thereafter, vector counterparts were obtained for polarization studies [20]. By using 3 + 3 beam-interference and holographic techniques, gradient-index-array and "dual-periodic motheye" photonic lattice fields were generated to fabricate bio-inspired microstructures that improve the anti-reflection for solar energy harvesting [21]. In addition, photonic supercrystals and super-quasi-crystals with complex gradients were obtained through pixel-by-pixel phase engineering in a spatial light modulator, which has potential application in light extraction efficiency and topological photonics [22,23].

Recently, in 2D materials, two materials were stacked together at a torsion angle under the action of van der Waals forces [24,25] to form a new type of artificial material referred to as moiré superlattices [26,27]. By adjusting the energy band structure, these materials exhibit novel physical properties [28]. Correspondingly, photonic moiré superlattice fields (periodic patterns resulting from the superposition of periodic structures that differ in frequency or orientation from each other) were designed using superposition suppresses and creates new features like defects (vacancies) and dark singularities [29,30]. Besides, two twisted discrete wavefields can also generate moiré wavefields [31]. Researchers observed that photonic moiré lattice exhibits a localization-delocalization transition that depends on the amplitude and twisted angle of the sublattice in the linear regime [32,33]. When a nonlinear regime was considered, photonic moiré lattices controlled the formation of spatial solitons [34]. The studies above show the broad potential of wave excitations with photonic gradient lattices and moiré lattices. However, to the best of our knowledge, the gradient structure of a photonic moiré lattice has not been studied.

In this study, we propose a method for obtaining gradient photonic moiré lattice fields by calculating the twisted angle of the periodic triangular moiré wavefields, which is similar to that of the hexagonal counterparts under the condition of $\Delta\alpha \in (0, \pi/6)$. This principle makes it possible to design gradient beams that contain three periodic structures as the basis of moiré fields. Further studies focusing on the geometric symmetry of the hexagonal moiré wavefields, where two special angles $\Delta\alpha|_{C=3}$ and $\Delta\alpha|_{C=5}$ are calculated, and whose corresponding wavefields have identical or swapped structures, but with a 30° bias, were conducted. On this basis, the arrangement of patterns in the gradient wavefields became more flexible. Finally, the experimental results revealed that the gradient wavefields can be obtained using the holographic method . In addition, the non-diffraction character was measured experimentally.

2. Design of gradient photonic moiré wavefields

According to [19], gradient moiré structures comprising three 2D periodic lattice fields were obtained as expressed in the following equation:

$$\boldsymbol{\psi}_G = \boldsymbol{\psi}_{6+6} - a \cdot \boldsymbol{\psi}_{3+3} - b \cdot \boldsymbol{\psi}'_{6+6}, \tag{1}$$

where $\boldsymbol{\psi}_{6+6}$, $\boldsymbol{\psi}_{3+3}$, and $\boldsymbol{\psi}'_{6+6}$ represent three child photonic moiré fields superposed by two hexagonal lattice fields, two triangular lattice fields, and two hexagonal lattice fields, respectively. Arguments a and b denote the amplitude factors of the latter two moiré fields with the following expression:

$$a, b = \begin{cases} 2x, 0, & 0 < x \le 0.5 \\ 0, x - 0.5, & 0.5 < x < 1 \end{cases}. \tag{2}$$

where x dominates the normalized coordinates. To ensure that the obtained photonic moiré field $\boldsymbol{\psi}_G$ has a gradient structure along the x axis and maintains periodicity in the orthogonal axis simultaneously, the moiré field $\boldsymbol{\psi}_{3+3}$ must be periodic and share an identical twisted angle with $\boldsymbol{\psi}_{6+6}$. When two lattice fields are coherently superimposed, the light fields can be expressed as

Optics EXPRESS

follows [31]:

$$\Psi_{N+N}(\mathbf{r}) = \sum_{j=1}^{N} \mathbf{E}_j e^{i(\mathbf{k}_j \cdot \mathbf{r} + \varphi_j)} + \sum_{j'=1}^{N} \mathbf{E}'_j e^{i\left(\mathbf{k}'_j \cdot \mathbf{r} + \varphi'_j\right)}, \tag{3}$$

where $\mathbf{E}_j$ and $\mathbf{E}'_j$ represent the amplitudes of the plane beams, whereas φ_j and φ'_j represent the initial phases. Term N denotes the number of plane beams, whereas $\mathbf{r}$ represents a position vector expressing $|\mathbf{r}| = \sqrt{x^2 + y^2 + z^2}$. To ensure the non-diffraction characteristics of the moiré field, the wave vectors $\mathbf{k}_j$ and $\mathbf{k}'_j$ are regulated as follows:

$$\begin{aligned} \mathbf{k}_j &= k\left[\cos\left(m_j\pi\right)\sin\theta, \sin\left(m_j\pi\right)\sin\theta, \cos\theta\right] \\ \mathbf{k}'_j &= k\left[\cos\left(m'_j\pi\right)\sin\theta, \sin\left(m'_j\pi\right)\sin\theta, \cos\theta\right] \end{aligned}, \tag{4}$$

where $k = 2\pi/\lambda$ and θ represent the wavenumber and tilt angle, respectively. The coefficients of the azimuthal angles are calculated as $m_j = (2j/N + \Delta\alpha/\pi)$ and $m'_j = (2j/N - \Delta\alpha/\pi)$, whose values affect the spectral distribution of the superimposed wavefield in the spectral space. $\Delta\alpha$ denotes the twisted angle of the triangular and hexagonal wavefields from the ξ axis (see Fig. 1), whereas j is a positive integer.

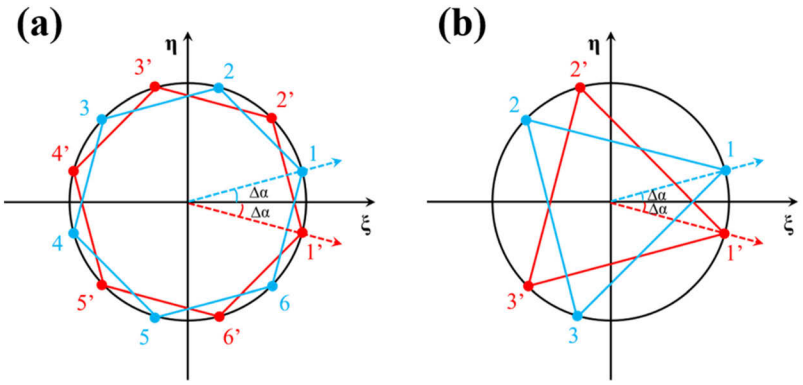

Fig. 1. Spectral components of superposition of two twisted light fields. Superposition of two hexagonal lattice light fields (a) and two triangular lattice light fields (b).

When two triangular light fields are superimposed, $N = 3$ exists, and the Fourier spectrum is shown in Fig. 1(b). The spectral components are recorded as $1,\ 1',\ 2,\ 2'$, and $3,\ 3'$, respectively. Thus, Eq. (3) can be expanded as follows:

$$\psi_{3+3}(x, y) = 2|\mathbf{E}| \sum_{j=1}^{3} \cos\left[k\sin\theta\cos\left(\frac{2j\pi}{3} + \Delta\alpha\right)x\right] \cos\left[k\sin\theta\sin\left(\frac{2j\pi}{3} + \Delta\alpha\right)y\right], \tag{5}$$

where $|\mathbf{E}|$ denotes the magnitude of the electric field vector. It can be observed from Eq. (5) that the superimposed light field has similar periods in the x and y directions.

According to Eq. (5), $\psi_{3+3}(x, y)$ represents the sum of three periodic functions with periods of $T_1 = 2\pi/(k\sin\theta\cos\Delta\alpha)$, $T_2 = 2\pi/[k\sin\theta\cos(\Delta\alpha + 2\pi/3)]$, and $T_3 = 2\pi/[k\sin\theta\cos(\Delta\alpha + \pi/3)]$, respectively. We assume that $T_2/T_3 = c_1$ and $T_3/T_1 = c_2$, and that $\psi_{3+3}(x, y)$ is a periodic

Optics EXPRESS

function when c_1 and c_2 are integers. The angle $\Delta\alpha$ can be deduced as follows:

$$\Delta\alpha = \begin{cases} \arctan\frac{\sqrt{3}}{3}\left(1-\frac{2}{c_1c_2}\right), \Delta\alpha \in \left(0, \frac{\pi}{6}\right) \\ \arctan\frac{\sqrt{3}}{3}\left(c_1^2c_2^2-1\right), \Delta\alpha \in \left(\frac{\pi}{6}, \frac{\pi}{3}\right) \end{cases}. \tag{6}$$

Considering the twisted angle of $\psi_{6+6}(x, y)$ [31], it is clear that the twisted angle of $\psi_{3+3}(x, y)$ is consistent with that of $\psi_{6+6}(x, y)$, under the condition of $\Delta\alpha \in \left(0, \frac{\pi}{6}\right)$. In Eq. (6), c_1c_2 is expressed by C within a range of $[2, +\infty)$. The change in C corresponds to the rotation of the hexagonal and triangular lattice fields whose spectral components are located in one circle, as depicted in Fig. 1. Therefore, the above discussion confirms that Eq. (1) can be used to design gradient photonic moiré wavefields.

3. Simulation and experimental results of gradient photonic moiré fields

Based on Eq. (1), three periodic moiré structures can be arranged in the gradient wavefields. When C is set at 3 and all the plane waves in the three child periodic beams are in-phase (for instance, zero-phase), the generated gradient wavefield is as shown in Figs. 2(d) and (e). Where (d) is the simulated phase diagram and (e) is the experimental intensity diagram. It is evident that the gradient photonic moiré field contains three periodic structures along the x axis, corresponding to the child moiré fields depicted in Figs. 2(a1-c1) (spectral components), (a2-c2) (phase diagrams), and (a3-c3) (intensity graphs), respectively. Among the three child wavefields, there are two hexagonal moiré fields superimposed by two simple hexagonal lattice beams [see Figs. 2(a1-a3)] and two honeycomb lattice fields [see Figs. 2(c1-c3)], respectively. In the middle of the gradient moiré wavefield, the structure corresponding to the moiré lattice field shown in Figs. 2(b1-b3) is composed of two triangular lattice beams with a twisted angle of $2\Delta\alpha|_{C=3}$. Numerical simulation and experimental results reveal that the triangular moiré lattice field is periodic when $C = 3$ is satisfied. In addition, although all the initial phases of plane waves that constitute the child moiré wavefields are zero, π phases emerge in the spectral component of the right hexagonal lattice field, as shown in Fig. 2(c1), which is different from that in Fig. 2(a1). This phenomenon originates from Eq. (1). In the in-phase situation, Eq. (1) represents the difference value of ψ_{6+6} and gradually increasing ψ_{3+3} when x is set at $(0, 0.5)$. If x is equal to 0.5, only ψ'_{3+3} exists as a result of $\psi_{6+6} - \psi_{3+3}$. In the right part of the gradient moiré field, the wavefield is the difference between ψ'_{3+3} and ψ'_{6+6}. Finally, the amplitudes corresponding to the spectral components of $2,\ 2', 4,\ 4'$, and $6,\ 6'$ are positive, whereas the components of $1,\ 1', 3,\ 3'$, and $5,\ 5'$ are negative. When x is equal to 1, the absolute values of all the amplitudes are similar, indicating that a π phase is induced in the spectral components with negative amplitudes.

Similarly, the gradient moiré wavefields contain three varying periodic moiré structures when the phases of adjacent spectral components are opposite, as shown in Fig. 3, respectively. The spectral components, phase diagrams, and intensity patterns of the three periodic moiré beams are as shown in Figs. 3(a1-c1), (a2-c2), and (a3-c3), respectively. From Fig. 3(a3), the coherence of two simple hexagonal lattice fields with inverse phases forms an intensity pattern consisting of periodic loops. Each loop comprised 12 light spots. The patterns in Figs. 3(b3) and (c3) are quite similar, but there are complex vortex structures in the phase diagram shown in Fig. 3(b2), yet no vortex phase exists in ψ'_{6+6} according to Fig. 3(c2). The spectral components are the same as in the case of in-phase superposition, where there is a π phase difference in plane beams $1,\ 1', 3,\ 3'$, and $5,\ 5'$ compared to ψ_{6+6} shown in Fig. 3(a1). As shown in Figs. 3(d) and (e), the generated gradient moiré wavefield contains three phase patterns in Figs. 3(a2-c2) and three intensity patterns in Figs. 3(a3-c3).

Optics EXPRESS

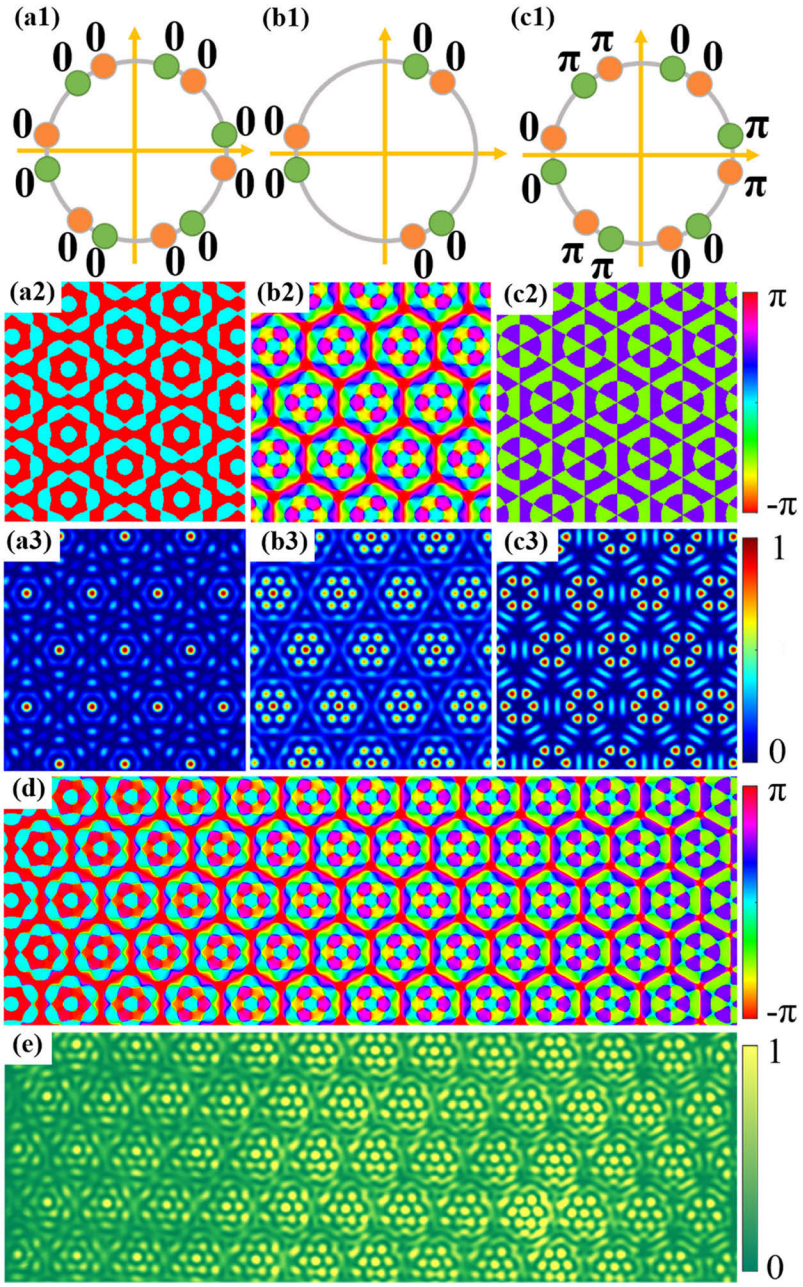

Fig. 2. Moiré lattice wavefield generated by in-phase superposition of two twisted hexagonal wavefields (a1-a3) and (c1-c3), and a triangular wavefield (b1-b3); (a1), (a2), and (a3) schematics of interferometric sources; (d) simulated phase diagram of gradient moiré lattice wavefield superposed by wavefields (a-c); (e) experimental intensity diagram of gradient moiré lattice wavefield superposed by wavefields (a-c).

Optics EXPRESS

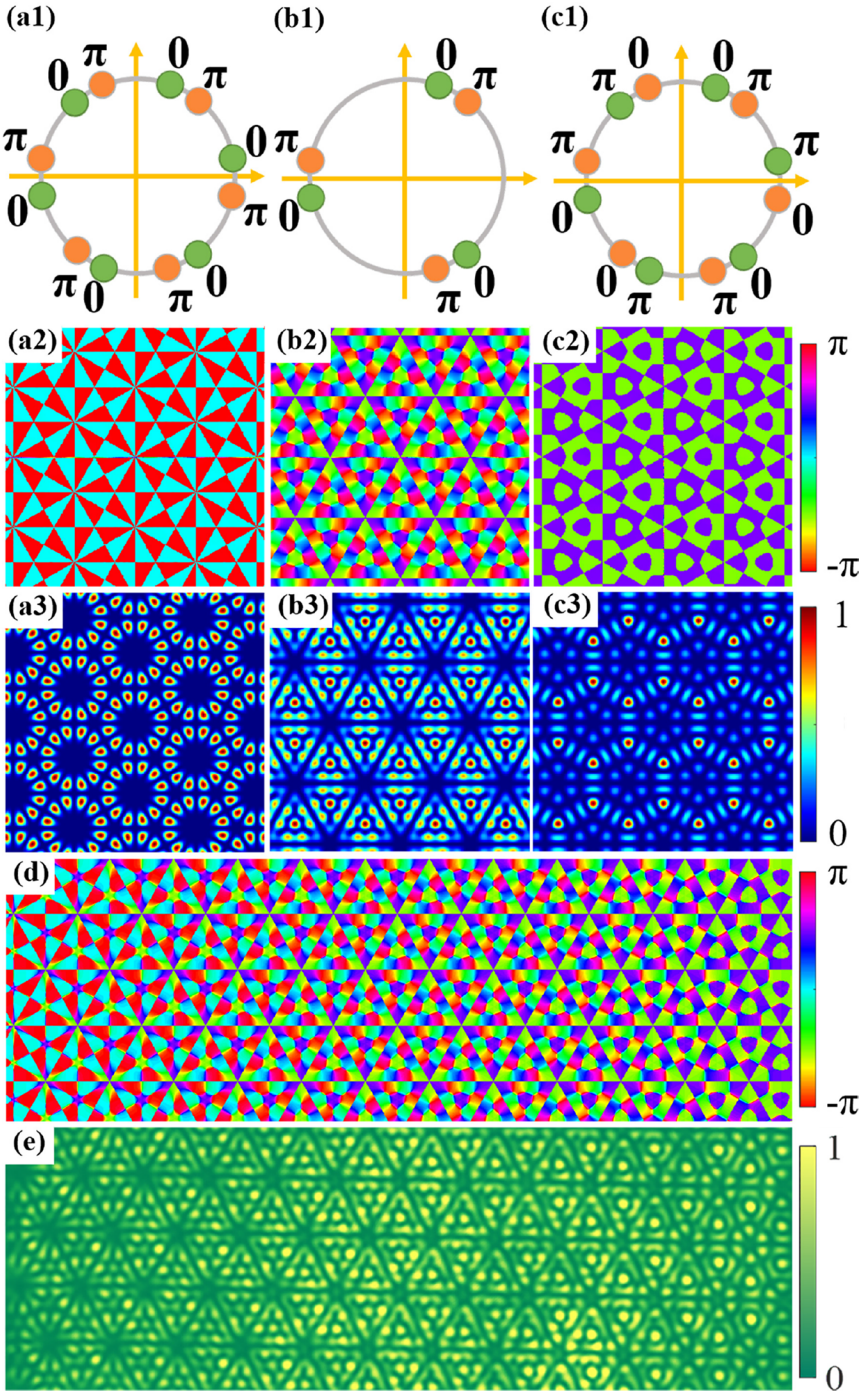

Fig. 3. Moiré lattice wavefield generated by out-phase superposition of two twisted hexagonal wavefields (a1-a3) and (c1-c3), and a triangular wavefield (b1-b3); (a1), (a2), and (a3) schematics of interferometric sources; (d) simulated phase diagram of gradient moiré lattice wavefield superposed by wavefields (a-c); (e) experimental intensity diagram of gradient moiré lattice wavefield superposed by wavefields (a-c).

Optics EXPRESS

4. Structural arrangement of the child moiré fields

In the previous section, all the child moiré fields are six-fold symmetric, indicating the existence of two varying twisted angles that generate identical moiré beam structures. Figures 4(a) and (b) show the spectral components of the child moiré fields with varying twisted angles $2\Delta\alpha_1$ and $2\Delta\alpha_2$. If the generated moiré fields are identical, the spectral components (including intensity and phase) in the red dotted box must be similar, resulting in the angles of $\Delta\alpha_1$ and $\Delta\alpha_2$ satisfying the following relation:

$$\Delta\alpha_1 + \Delta\alpha_2 = 30^\circ. \tag{7}$$

Once Eq. (7) is satisfied, there is a 30° bias between the spectral components in the two red dotted boxes [see Figs. 4(a1) and (b1)]. According to the periodic condition of the moiré fields, the following hold:

$$\begin{cases} \tan\alpha_1 = \frac{\sqrt{3}}{3}(1 - \frac{2}{C_1}) \\ \tan\alpha_2 = \frac{\sqrt{3}}{3}(1 - \frac{2}{C_2}) \end{cases} \tag{8}$$

Combining Eqs. (7) and 8, one can easily determine the following relation:

$$C_2 = 2 + \frac{3}{C_1 - 2}. \tag{9}$$

The periodic condition of moiré lattice fields limits the values of C_1 and C_2 are integers in $[2, +\infty)$; thus, there are two solutions to Eq. (9), which are $C_1 = 3$ and $C_2 = 5$ or $C_1 = 5$ and $C_2 = 3$.

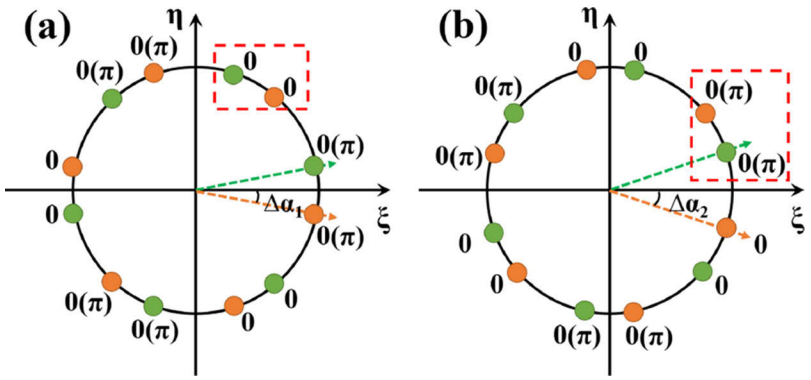

Fig. 4. Geometric symmetry of the child moiré fields. Schematic of the superposition source with a twisted angle of $2\Delta\alpha_1 = 2\Delta\alpha|_{C=3}$ (a) and $2\Delta\alpha_2 = 2\Delta\alpha|_{C=5}$ (b) .

In Fig. 5, all the moiré lattice fields with six-fold symmetry (rotational symmetry of order 6) are displayed when the phases of the plane waves are 0 or π. In addition, according to the above calculation, we set the twisted angles of sub-wavefields $2\Delta\alpha|_{C=3}$ [upper two rows] and $2\Delta\alpha|_{C=5}$ (bottom two rows), respectively. In comparison with Figs. 5(a2) and (g2), if the phases of plane waves are zero, the structures of the two moiré fields coincide with only a 30° bias. The same situation exists when the phases of the plane waves are $\{0, \pi, 0, \pi, \cdots\}$ [see Figs. 5(b2) and (h2)]. This phenomenon is consistent with the above calculation. Otherwise, the structures of the moiré lattice fields with plane wave phases of $\{0, 0, \pi, \pi, \cdots\}$ in Fig. 5(c1) and $\{0, \pi, \pi, 0, \cdots\}$ in Fig. 5(d1) are identical to those in Figs. 5(j1) and (i1). For triangular moiré lattice fields, as shown in Figs. 5(e1-f1) and (k1-l1), there is no clear similarity between the two twisted angles.

In the previous section, the gradient moiré wavefield generated by in-phase superposition contains two hexagonal child moiré structures, as shown in Figs. 5(a2) and (c2), and the triangular

Optics EXPRESS

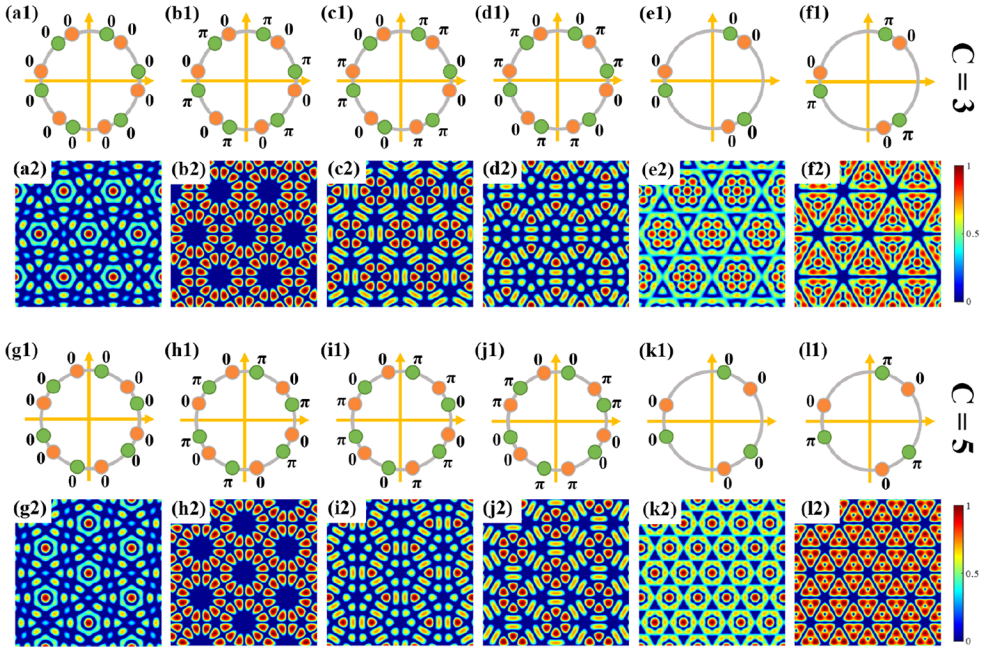

Fig. 5. Child moiré lattice wavefields with two twisted angles and different phases. Optical source distributions (a1-d1) and intensity patterns (a2-d2) of child moiré lattice wavefields superimposed by two hexagonal wavefields with a twisted angle of $2\Delta\alpha_1 = 2\Delta\alpha|_{C=3}$; optical source distributions (e1-f1) and intensity patterns (e2-f2) of child moiré lattice wavefields superimposed by two triangular wavefields with a twisted angle of $2\Delta\alpha_1 = \Delta\alpha|_{C=3}$. Bottom two rows correspond to the upper two rows with a twisted angle of $2\Delta\alpha_1 = 2\Delta\alpha|_{C=5}$.

structure is shown in Fig. 5(e2). The out-phase superimposed counterpart contained two hexagonal moiré structures [Figs. 5(b2) and (d2)], as well as triangular [Fig. 5(f2)]. Based on the principle shown in Fig. 5, a new arrangement that contains Figs. 5(a2) and (d2) can be designed by altering the twisted angle to $2\Delta\alpha_1 = 2\Delta\alpha|_{C=5}$ and 30° rotation, based on the in-phase superposition in Fig. 2. The phase and intensity distribution corresponding to the gradient moiré wavefields are shown in Figs. 6(a2) and (a3), where the triangular child moiré wavefield corresponds to that in Fig. 5(k2). Similarly, the assembly of the two hexagonal child moiré wavefields in Figs. 5(b2) and (c2) are achieved based on the out-phase superposition in Fig. 3, as shown in Fig. 6(b3). In this gradient moiré wavefield, the intermediate triangular structure corresponds to that shown in Fig. 5(l2). The remaining combinations of the hexagonal moiré wavefield are shown in Figs. 5(a2) and (b2), as well as in Figs. 5(c2) and (d2). According to the relation of the left and right hexagonal structures, the phases of plane beams for generating intermediate wavefields remain invariant, whereas those of others possess a π phase change. Therefore, to achieve both residual combinations, the intermediate structures belong to the hexagonal lattice wavefields. From Fig. 6(c3), it is clear that the two hexagonal moiré wavefields in Figs. 5(a2) and (b2) are arranged together. In addition, the intermediate structure is a hexagonal lattice wavefield. Using the same method, the two hexagonal moiré wavefields shown in Figs. 5(c2) and (d2) are combined, and the intermediate structure is a honeycomb lattice wavefield, as shown in Fig. 6(d3).

Optics EXPRESS

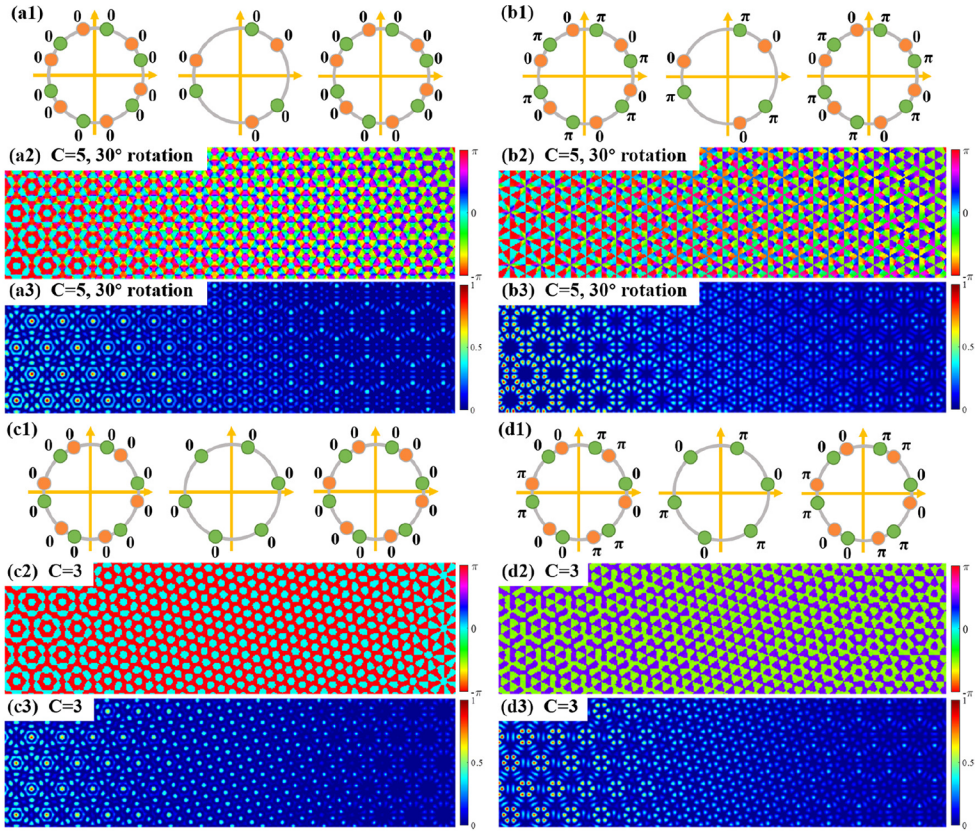

Fig. 6. Gradient wavefields with controllable moiré patterns. In-phase (a1-a3) and (b1-b3) out-phase superposition of three moiré lattice wavefields with a twisted angle of $2\Delta\alpha_1 = \Delta\alpha|_{C=5}$; (c1-c3) and (d1-d3) superposition wavefields containing the moiré patterns in Figs. 5(a2) and (b2), as well as Figs. 5(c2) and (d2), respectively.

5. Experimental setup and non-diffraction characteristics of gradient moiré wavefields

In this study, the gradient structures were superimposed by three child moiré lattice fields. The complex intensities and phases of the interference beams make it difficult to achieve them using simple intensity and phase masks. Therefore, the holographic method, which is also known as the one-step imaging method, is utilized to generate these light fields. The experimental setup is shown in Fig. 7. A continuous-wave laser beam with a wavelength of 532 nm passes through lenses L_1 and L_2 to be expanded as a parallel beam. The beam thereafter passes through the polarizer LP_1 to irradiate the phase-only spatial light modulator (SLM), and the modulated light is subsequently filtered by a 4f system to produce the required gradient wavefields. Finally, the intensity distributions of the wavefields were recorded using a CCD camera near the back focal plane of the 4f system. In the setup, the SLM controlled by a computer was utilized to perform the gray phase diagrams of the simulated gradient wavefields, as shown in the blue box in Fig. 7(a). The phase diagrams in Figs. 2(d), 3(d) and 6(a2-d2) are used to generate the corresponding gradient wavefields after being converted into gray images. If there is no phase diagram in the SLM, there is only one bright spot on the spectral plane of the 4f system, whereas several bright spots emerge around the central spot [see Figs. 7(b) and (c)]. In the spectral plane, a circular filter was used to percolate 12 bright spots between the two white circles in Fig. 7(c).

Optics EXPRESS

In addition, two polarizers, LP_1 and LP_2, with orthogonal polarization directions, were used to eliminate the background light to improve the contrast ratio of the gradient wavefields.

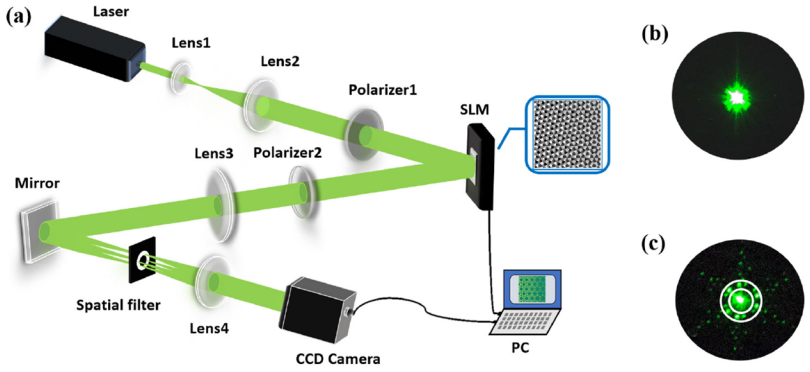

Fig. 7. Schematic of experimental setup on non-diffraction gradient moiré wavefields (a); (b) and (c) spectral distribution without and with phase diagram in SLM, respectively. CCD: charge coupled device; SLM: spatial light modulator; PC: personal computer.

The spectral components of the generated gradient moiré lattice fields are located on a circle, thereby maintaining the non-diffraction characteristic. The simulated results are as shown in Fig. 8(a). To verify the non-diffraction property of the generated gradient moiré wavefields in the experiment, the CCD camera is shifted along the z axis and it records the wavefield at different positions at the front and back of the back focal plane of the 4f system. The cross-sections of the simulation results are selected at the corresponding positions and compared with the experimental results [see Fig. 8(b)]. The gradient structure of the light field maintains its pattern from f_0-6 to f

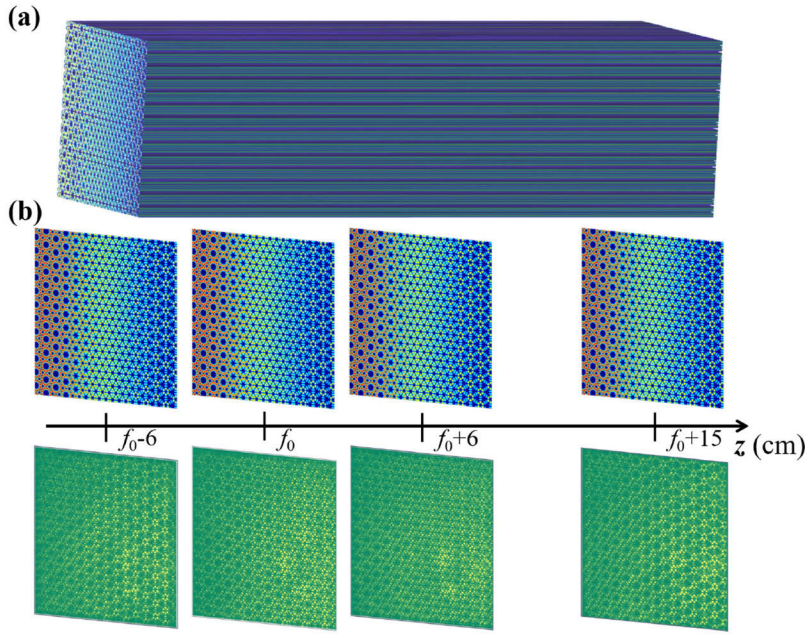

Fig. 8. Non-diffraction transmission of gradient moiré wavefield by (a) simulation and (b) comparison of light cross-sections between simulation and experimental results.

Optics EXPRESS

$_0$+15 cm, indicating that the nondiffracting length of the generated gradient moiré lattice field is at least 21 cm. Generally, the thickness of the photorefractive crystal used to fabricate photonic lattices is less than 10 mm; thus, the gradient moiré lattice fields satisfy the requirements of studying light modulation in photonic lattices.

6. Conclusion

We deduce the periodic condition of the triangular moiré lattice field, which is coincident with that of the hexagonal moiré wavefield if the angle $\Delta\alpha$ is in the range $(0, \frac{\pi}{6})$. Based on the precondition, the gradient moiré wavefields containing three periodic child moiré patterns superimposed by hexagonal, triangular, and hexagonal wavefields are easily obtained. Three-child photonic moiré wavefields generated by in-phase and out-phase superposition are coherently stacked to generate different gradient photonic moiré beams. In addition, for the hexagonal moiré wavefields, with proper phase modulation, their intensity patterns with $\Delta\alpha|_{C=3}$ are identical to those with $\Delta\alpha|_{C=5}$. This principle increases the flexibility of arranging the child moiré lattice fields. Experimental results demonstrate that the designed gradient photonic moiré lattice fields can be achieved by using the holographic method, and the nondiffracting length of the gradient wavefield is measured to be at least 21 cm. Existing experiments have proved that the non-diffraction wavefields can be used to make photonic lattices in photorefractive crystals, and the refractive index of photorefractive crystals is sensitive to light intensity. Therefore, the obtained gradient photonic moiré lattice fields have great potential in two-dimensional photonic lattices and moiré quasicrystals, enhancing the ability of light control and new optical devices.

Funding. National Natural Science Foundation of China (91950104, 11974218).

Disclosures. The authors declare no conflicts of interest.

Data availability. Data underlying the results presented in this paper are not publicly available at this time but may be obtained from the authors upon reasonable request.

References

1. D. N. Christodoulides, F. Lederer, and Y. Silberberg, "Discretizing light behaviour in linear and nonlinear waveguide lattices," Nature **424**(6950), 817–823 (2003).
2. C. R. Rosberg, D. N. Neshev, A. A. Sukhorukov, W. Krolikowski, and Y. S. Kivshar, "Observation of nonlinear self-trapping in triangular photonic lattices," Opt. Lett. **32**(4), 397–399 (2007).
3. S. Xia, A. Ramachandran, S. Xia, D. Li, X. Liu, L. Tang, Y. Hu, D. Song, J. Xu, D. Leykam, S. Flach, and Z. Chen, "Unconventional flatband line states in photonic lieb lattices," Phys. Rev. Lett. **121**(26), 263902 (2018).
4. H. Martin, E. D. Eugenieva, Z. Chen, and D. N. Christodoulides, "Discrete solitons and soliton-induced dislocations in partially coherent photonic lattices," Phys. Rev. Lett. **92**(12), 123902 (2004).
5. J. W. Fleischer, M. Segev, N. K. Efremidis, and D. N. Christodoulides, "Observation of two-dimensional discrete solitons in optically induced nonlinear photonic lattices," Nature **422**(6928), 147–150 (2003).
6. Z. Chen, H. Martin, A. Bezryadina, D. Neshev, Y. S. Kivshar, and D. N. Christodoulides, "Experiments on gaussian beams and vortices in optically induced photonic lattices," J. Opt. Soc. Am. B **22**(7), 1395–1405 (2005).
7. M. Boguslawski, P. Rose, and C. Denz, "Increasing the structural variety of discrete nondiffracting wave fields," Phys. Rev. A **84**(1), 013832 (2011).
8. Z. Chen, H. Martin, E. D. Eugenieva, J. Xu, and J. Yang, "Formation of discrete solitons in light-induced photonic lattices," Opt. Express **13**(6), 1816–1826 (2005).
9. M. Boguslawski, P. Rose, and C. Denz, "Nondiffracting kagome lattice," Appl. Phys. Lett. **98**(6), 061111 (2011).
10. Z. Bouchal, "Nondiffracting optical beams: Physical properties, experiments, and applications," Czech. J. Phys. **53**(7), 537–578 (2003).
11. P. Rose, M. Boguslawski, and C. Denz, "Nonlinear lattice structures based on families of complex nondiffracting beams," New J. Phys. **14**(3), 033018 (2012).
12. J. Xavier, P. Rose, B. Terhalle, J. Joseph, and C. Denz, "Three-dimensional optically induced reconfigurable photorefractive nonlinear photonic lattices," Opt. Lett. **34**(17), 2625–2627 (2009).
13. S. Behera, S. Sarkar, and J. Joseph, "Fabrication of helical photonic structures with submicrometer axial and spatial periodicities following "inverted umbrella" geometry through phase-controlled interference lithography," Opt. Lett. **43**(1), 106–109 (2018).
14. X. Dong, Q. Ya, X. Sheng, Z. Li, Z. Zhao, and X. Duan, "Photonic bandgap of gradient quasidiamond lattice photonic crystal," Appl. Phys. Lett. **92**(23), 231103 (2008).
15. E. Centeno and D. Cassagne, "Graded photonic crystals," Opt. Lett. **30**(17), 2278–2280 (2005).

Optics EXPRESS

16. H. Kurt and D. S. Citrin, "Graded index photonic crystals," Opt. Express **15**(3), 1240–1253 (2007).
17. F. Gaufillet and E. Akmansoy, "Design and experimental evidence of a flat graded-index photonic crystal lens," J. Appl. Phys. **114**(8), 083105 (2013).
18. F. S. Roux and I. De Leon, "Planar photonic crystal gradient index lens, simulated with a finite difference time domain method," Phys. Rev. B **74**(11), 113103 (2006).
19. M. Kumar and J. Joseph, "Generating a hexagonal lattice wave field with a gradient basis structure," Opt. Lett. **39**(8), 2459–2462 (2014).
20. S. K. Pal and P. Senthilkumaran, "Hexagonal vector field of polarization singularities with a gradient basis structure," Opt. Lett. **44**(8), 2093–2096 (2019).
21. S. Behera and J. Joseph, "Single-step optical realization of bio-inspired dual-periodic motheye and gradient-index-array photonic structures," Opt. Lett. **41**(15), 3579–3582 (2016).
22. D. Lowell, S. Hassan, O. Sale, M. Adewole, N. Hurley, U. Philipose, B. Chen, and Y. Lin, "Holographic fabrication of graded photonic super-quasi-crystals with multiple-level gradients," Appl. Opt. **57**(22), 6598–6604 (2018).
23. O. Sale, S. Hassan, N. Hurley, K. Alnasser, U. Philipose, H. Zhang, and Y. Lin, "Holographic fabrication of octagon graded photonic supercrystal and potential applications in topological photonics," Front. Optoelectronics **13**(1), 12–17 (2020).
24. Y. Cao, V. Fatemi, A. Demir, S. Fang, S. L. Tomarken, J. Y. Luo, J. D. Sanchez-Yamagishi, K. Watanabe, T. Taniguchi, E. Kaxiras, R. C. Ashoori, and P. Jarillo-Herrero, "Correlated insulator behaviour at half-filling in magic-angle graphene superlattices," Nature **556**(7699), 80–84 (2018).
25. Y. Cao, V. Fatemi, S. Fang, K. Watanabe, T. Taniguchi, E. Kaxiras, and P. Jarillo-Herrero, "Unconventional superconductivity in magic-angle graphene superlattices," Nature **556**(7699), 43–50 (2018).
26. S. S. Sunku, G. X. Ni, B. Y. Jiang, H. Yoo, A. Sternbach, A. S. Mcleod, T. Stauber, L. Xiong, T. Taniguchi, and K. Watanabe, "Photonic crystals for nano-light in moiré graphene superlattices," Science **362**(6419), 1153–1156 (2018).
27. O. Vafek and J. Kang, "Renormalization group study of hidden symmetry in twisted bilayer graphene with coulomb interactions," Phys. Rev. Lett. **125**(25), 257602 (2020).
28. G. Abbas, Y. Li, H. Wang, W.-X. Zhang, C. Wang, and H. Zhang, "Recent advances in twisted structures of flatland materials and crafting moiré superlattices," Adv. Funct. Mater. **30**(36), 2000878 (2020).
29. M. Kumar and J. Joseph, "Embedding a nondiffracting defect site in helical lattice wave-field by optical phase engineering," Appl. Opt. **52**(23), 5653–5658 (2013).
30. S. K. Pal and P. Senthilkumaran, "Lattice of c points at intensity nulls," Opt. Lett. **43**(6), 1259–1262 (2018).
31. Y. Gao, Z. Wen, L. Zheng, and L. Zhao, "Complex periodic non-diffracting beams generated by superposition of two identical periodic wave fields," Opt. Commun. **389**, 123–127 (2017).
32. C. Huang, F. Ye, X. Chen, Y. V. Kartashov, V. V. Konotop, and L. Torner, "Localization-delocalization wavepacket transition in pythagorean aperiodic potentials," Sci. Rep. **6**(1), 32546 (2016).
33. P. Wang, Y. Zheng, X. Chen, C. Huang, Y. V. Kartashov, L. Torner, V. V. Konotop, and F. Ye, "Localization and delocalization of light in photonic moiré lattices," Nature **577**(7788), 42–46 (2020).
34. Q. Fu, P. Wang, C. Huang, Y. V. Kartashov, L. Torner, V. V. Konotop, and F. Ye, "Optical soliton formation controlled by angle twisting in photonic moiré lattices," Nat. Photonics **14**(11), 663–668 (2020).